X-ray Magnetic Circular Dichroism in Altermagnetic α-MnTe

A. Hariki,[1] T. Yamaguchi,[1] D. Kriegner,[2] K. W. Edmonds,[3] P. Wadley,[3] S. S. Dhesi,[4] G. Springholz,[5] L. Šmejkal,[6,2] K. Výborný,[2] T. Jungwirth,[2,3] and J. Kuneš[7]

[1]*Department of Physics and Electronics, Graduate School of Engineering, Osaka Metropolitan University, 1-1 Gakuen-cho, Nakaku, Sakai, Osaka 599-8531, Japan*
[2]*Institute of Physics, Czech Academy of Sciences, Cukrovarnická 10, 162 00 Praha 6 Czech Republic*
[3]*School of Physics and Astronomy, University of Nottingham, Nottingham NG7 2RD, United Kingdom*
[4]*Diamond Light Source, Chilton OX11 0DE, United Kingdom*
[5]*Institute of Semiconductor and Solid State Physics, Johannes Kepler University Linz, Altenbergerstr. 69, 4040 Linz, Austria*
[6]*Institut für Physik, Johannes Gutenberg Universität Mainz, D-55099 Mainz, Germany*
[7]*Institute for Solid State Physics, TU Wien, 1040 Vienna, Austria*

Altermagnetism is a recently identified magnetic symmetry class combining characteristics of conventional collinear ferromagnets and antiferromagnets, that were regarded as mutually exclusive, and enabling phenomena and functionalities unparalleled in either of the two traditional elementary magnetic classes. In this work we use symmetry and *ab initio* theory to explore X-ray magnetic circular dichroism (XMCD) in the altermagnetic class. Our results highlight the distinct phenomenology in altermagnets of this time-reversal symmetry breaking response, and its potential utility for element-specific spectroscopy and microscopy in altermagnets. As a representative material for our XMCD study we choose α-MnTe with the compensated antiparallel magnetic order in which an anomalous Hall effect has been already demonstrated both in theory and experiment. The predicted magnitude of XMCD lies well within the resolution of existing experimental techniques.

Recent theoretical studies have identified magnetic crystals with unconventional characteristics. On one hand, the crystal symmetries generate a compensated antiparallel magnetic order. On the other hand, they enable time-reversal ($\mathcal{T}$) symmetry breaking linear responses, such as the anomalous Hall effect (AHE) [1–10] or charge-spin conversion effects [2, 11–16], and strongly spin-polarized electronic band structures [2, 3, 6, 8, 16–23]. Theoretical predictions have gone beyond the previously established notion in which these $\mathcal{T}$-symmetry breaking phenomena originate from a magnetization in ferromagnets, or from a non-collinear order of spins on certain lattices of magnetic atoms [1]. *Ab initio* calculations in RuO_2 or MnTe have identified large non-relativistic spin splittings in the band-structure reaching an $\sim$ eV scale [2, 3, 9, 17]. In contrast to ferromagnets, and in line with the vanishing net magnetization in these compensated collinear magnets, the sign of the spin splitting alternates across the band structure. The alternating spin polarization in both real-space crystal structure and momentum-space electronic structure suggested the term altermagnetism [2, 16].

Prompted by the theory predictions, the AHE has already been experimentally observed and ascribed to the altermagnetic order in RuO_2 or MnTe [9, 24]. The predictions of strong spin currents, opening the prospect of robust writing and readout mechanisms in stray-field-free ultra-fast memory devices [2, 12, 15, 16, 25], have been supported by initial experiments in RuO_2 [26–28].

In this Letter we focus on the X-ray magnetic circular dichroism (XMCD) at the Mn $L_{2,3}$ edge and demonstrate that, apart from the ferromagnetic or non-collinear order [29, 30], it can also originate from the collinear altermagnetic order. Both AHE, the transverse electric-current response to an applied electric bias, and XMCD, the difference between absorption of left and right circularly polarized X-rays, are given by the Hall vector $\mathbf{h} = (\sigma_{zy}, \sigma_{xz}, \sigma_{yx})$; here $\sigma_{ij} = -\sigma_{ji}$ are the antisymmetric components of the (frequency dependent) conductivity tensor [1, 29]. AHE and XMCD are, therefore, governed by the same symmetry principles. Microscopically,

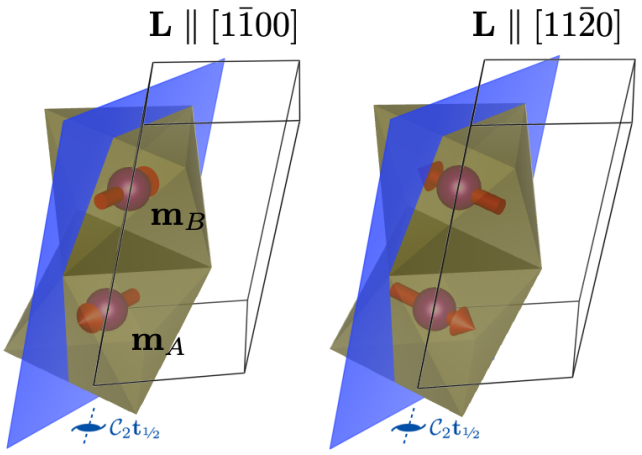

FIG. 1. Mn moments $\mathbf{m}_A$ and $\mathbf{m}_B$ in α-MnTe structure (with Te octahedra) for the studied Néel vector $\mathbf{L}$ orientations. The mirror plane $\mathcal{M}$ discussed in the text is marked in blue. While in the right panel $\mathcal{M}$ is an element of the magnetic symmetry groupk, in the left panel it is $\mathcal{MT}$ which leaves the system invariant.

they provide complementary information since XMCD involves, besides the valence electronic states, also the atomic core states.

Before presenting our microscopic calculations of XMCD in α-MnTe, we summarize key symmetry considerations relevant to altermagnets. We start from non-relativistic spin symmetries which consist of direct products of transformations in decoupled real (orbital) space and spin space and classify all crystals with collinear magnetic order into the following three mutually exclusive symmetry types [2, 16]: First, a ferromagnetic (ferrimagnetic) class has one spin lattice or opposite-spin sublattices not connected by any symmetry transformation, i.e., there is no symmetry combining a 180° spin-space rotation ($\mathcal{C}_2^S$) with any real-space symmetry transformation. Next, an antiferromagnetic class has opposite-spin sublattices connected by a real-space translation or inversion [31, 32]. Finally, an altermagnetic class has opposite-spin sublattices connected by a real-space rotation (proper or improper and symmorphic or non-symmorphic), but not connected by a translation or inversion. Unlike the ferromagnetic class with a non-relativistic magnetization and spin-polarized bands that break $\mathcal{T}$-symmetry, and unlike the antiferromagnetic class with non-relativistic zero net magnetization and spin-unpolarized $\mathcal{T}$-invariant bands, altermagnets have non-relativistic zero net magnetization combined with spin-polarized bands that break $\mathcal{T}$-symmetry. The non-relativistic altermagnetic symmetries thus suggest the presence of $\mathcal{T}$-symmetry breaking responses analogous to ferromagnets. Simultaneously, the spin symmetries point to qualitative difference in the phenomenology of these responses between ferromagnets and the intrinsically anisotropic (even-parity d, g or i-wave) altermagnets [2, 16, 17].

Besides the above non-relativistic spin symmetries that distinguish the three collinear magnetic classes, there are spin symmetries common to all collinear magnets. First, it is an arbitrary rotation of the spin space around the direction of ordered moments. Second, all collinear (coplanar) magnets share a $\mathcal{C}_2^S\mathcal{T}$ non-relativistic spin symmetry combining the spin-space inversion, i.e. the $\mathcal{T}$ transformation, with the $\mathcal{C}_2^S$ spin-space rotation around an axis perpendicular to the ordered moments. In the absence of the relativistic spin-orbit coupling (SOC), the Hall vector is invariant under arbitrary spin-space rotations, including the $\mathcal{C}_2^S$ rotation. Since collinear magnets are invariant under the above non-relativistic $\mathcal{C}_2^S\mathcal{T}$ spin-space symmetry, the Hall vector must be also invariant under this symmetry. Combined with the invariance under the spin-space rotation, the Hall vector is forced to be $\mathcal{T}$-invariant, i.e., to vanish in the absence of SOC.

In relativistic physics, the real space and the spin space are coupled eliminating pure spin rotations as well as the $\mathcal{C}_2^S\mathcal{T}$ spin-space symmetry. In ferromagnets, the Hall vector is then always allowed in the presence of SOC because both the magnetization and the Hall vector transform as $\mathcal{T}$-odd axial vectors [16]. In altermagnets, the symmetry lowering by SOC also enables the presence of the Hall vector, but not necessarily for all directions of the Néel vector. This is because the Néel vector may or may not transform as a $\mathcal{T}$-odd axial vector, depending on its crystal direction [16]. In the latter case, the relativistic symmetry lowering may not be sufficient to allow for the $\mathcal{T}$-odd axial Hall vector [2, 16]. This highlights the distinct phenomenology of AHE and XMCD in altermagnets compared to ferromagnets.

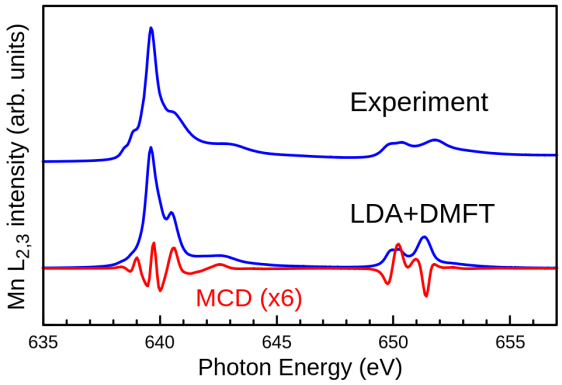

FIG. 2. Mn $L_{2,3}$ XAS experimental spectrum (top, blue) and the LDA+DMFT AIM calculation (bottom, blue). The XMCD predicted by the LDA+DMFT AIM for $\mathbf{L} \parallel [1\bar{1}00]$ (red). Here XMCD is given by σ_{yx} ($\mathbf{k} \parallel \mathbf{c} \perp \mathbf{L}$).

We now proceed to the analysis of the XMCD in MnTe. A schematic crystal of α-MnTe with NiAs structure (crystallographic space group $P6_3/mmc$ #194 [33]) is shown in Fig. 1. The magnetic moments on Mn have a parallel alignment within the c-planes and an antiparallel alignment between the planes. The face-sharing Te octahedra surrounding the Mn atoms break the translation or inversion symmetry connecting the opposite-spin sublattices, but allow a non-symmorphic six-fold screw rotation $\mathcal{C}_6^R t_{1/2}$ to connect them [9, 16] rendering α-MnTe an altermagnet.

The X-ray absorption spectrum (XAS) and XMCD at the Mn $L_{2,3}$ edge are calculated using a dynamical mean-field theory (DMFT) + Anderson impurity model (AIM) approach of Refs. 34–36. Starting with a density functional calculation using Wien2k [37] we construct a multiband Hubbard model [38, 39] spanning the Mn $3d$ and Te $5p$ bands. The Coulomb interaction within the Mn d-shell is parametrized by $U = 5.0$ eV and $J = 0.86$ eV, and the double-counting correction $\mu_{\rm dc} = 22.5$ eV. DMFT with these parameters reproduces well the valence-band both in experiment [40] and theory [41] as well as Mn $2p$ core-level x-ray photoemission spectra [42], see SM [43].

In Fig. 2 we compare the calculated XAS with the experiment. The measurements were performed on an epitaxial α-MnTe thin film grown on a InP (111) substrate

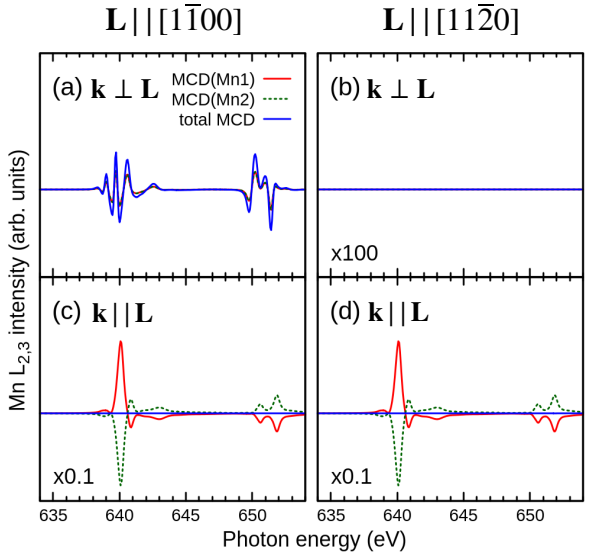

FIG. 3. The Mn site-resolved contributions to XMCD calculated by the LDA+DMFT AIM for two Néel vectors $\mathbf{L} = [1\bar{1}00]$ (left) and $[11\bar{2}0]$ (right). The top and bottom panels correspond to $\mathbf{k} \perp \mathbf{L}$ and $\mathbf{k} \parallel \mathbf{L}$, respectively. The XMCD intensities are magnified by a factor indicated in panels.

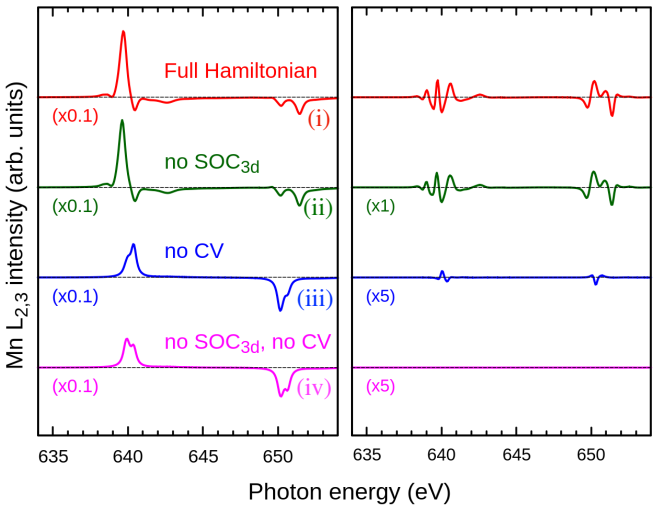

FIG. 4. The single-site XMCD for $\mathbf{k} \parallel \mathbf{L}$ (left) and $\mathbf{k} \perp \mathbf{L}$ (right) for models (i)-(iv) described in the text. The XMCD intensities are magnified by a factor indicated in panels. Note that here the Mn atomic model is employed.

by molecular beam epitaxy as described in Ref. 44. Samples were transported from the growth chamber to beamline I06 at Diamond Light Source in a vacuum suitcase. The XAS measurements we performed using linearly polarized light propagating along the c-axis. The polarization of the light was along the $[11\bar{2}0]$ direction and the measurement was performed at 200 K. Total electron yield detection was used to measure the absorption signal. All features seen in the experimental spectra are correctly reproduced; the only apparent exception is the multiplet feature on the low-energy side of the L_3 absorption edge, see SM [43] for discussion.

The main quantitative prediction of this work is in Fig. 2 showing the XMCD spectrum calculated for the Néel vector $\mathbf{L} = \mathbf{m}_A - \mathbf{m}_B$ parallel to $[1\bar{1}00]$. Here $\mathbf{m}_{A(B)}$ is the sublattice $A(B)$ magnetization, and $[1\bar{1}00]$ is one of the three equivalent magnetic easy-axes in the c-plane [9, 44]. The relativistic magnetic point group for this Néel vector direction is $m'm'm$ [9]. The screw axis $\mathcal{C}_2 t_{1/2}$ and the corresponding symmetry-allowed Hall vector $\mathbf{h} = (0, 0, \sigma_{yx})$ are along the crystal c-axis. In contrast, for $\mathbf{L}$ parallel to an in-plane hard axis $[2\bar{1}\bar{1}0]$, the corresponding magnetic point group mmm implies that all Hall vector components are zero, i.e., that a net XMCD signal is excluded by symmetry. Note that experimentally, the Néel vector can be reoriented within the c-plane by moderate magnetic fields [44].

Thanks to the localized nature of the core states, X-ray spectra are the sum of contributions from distinct atomic sites, i.e., from the magnetic sublattices A and B in the present case: $\sigma_{\alpha\beta} = \sigma^A_{\alpha\beta} + \sigma^B_{\alpha\beta}$. For Néel vector directions in the c-plane of α-MnTe, the sublattices A and B are connected by the relativistic $\mathcal{C}_2 t_{1/2}$ symmetry, which leads to $\sigma^A_{yx} = \sigma^B_{yx}$, $\sigma^A_{zy} = -\sigma^B_{zy}$ and $\sigma^A_{xz} = -\sigma^B_{xz}$.

The calculated site-resolved contributions to XMCD for $\mathbf{L}$ along $[1\bar{1}00]$ and $[11\bar{2}0]$ are shown in Fig. 3. We associate the x-axis of the conductivity tensor with the direction of $\mathbf{L}$. For both Néel vector directions, the two sublattices taken separately yield large local XMCD signals from $\sigma^{A(B)}_{zy}$ (i.e. for X-ray propagation vector $\mathbf{k} \parallel \mathbf{L}$), which cancel each other exactly when summed over. For XMCD given by σ_{yx} (X-ray propagation vector $\mathbf{k} \perp \mathbf{L}$), the identical contributions $\sigma^{A(B)}_{yx}$ of the two sublattices are finite for $\mathbf{L} \parallel [1\bar{1}00]$, and add up constructively. For $\mathbf{L} \parallel [11\bar{2}0]$, $\sigma^{A(B)}_{yx} = 0$ by symmetry.

The Onsager relations for the conductivity [1], and correspondingly for XMCD, imply that XMCD($\mathbf{L}$,$\mathbf{m}$)=−XMCD($-\mathbf{L}$,$-\mathbf{m}$). For $\mathbf{L} \parallel [1\bar{1}00]$ in α-MnTe, a net magnetization $\mathbf{m} = \mathbf{m}_A + \mathbf{m}_B$ due to canting of the sublattice moments towards the c-axis is allowed by the relativistic symmetry. It was estimated to be extremely small $\leq 2 \times 10^{-4}$ μB per Mn from *ab initio* calculations, and remained experimentally undetectable in the thin-film MnTe epilayers [9]. This implies a nearly precise relationship, XMCD($\mathbf{L}$)=−XMCD($-\mathbf{L}$).

While XMCD and AHE follow the same symmetry rules, they may originate from different terms in the Hamiltonian and thus have different magnitudes or scale differently upon changing the material parameters. An example of such a behavior is different magnitudes of MCD in optical and x-ray regimes related to their origin in valence-band and core-level SOC, respectively.

For $\mathbf{L} \parallel [1\bar{1}00]$ in α-MnTe, and the corresponding net XMCD given by σ_{yx}, it is instructive to analyze the

single-site XMCD contributions given by $\sigma_{yx}^{A(B)}$ ($\mathbf{k} \perp \mathbf{L}$) and $\sigma_{zy}^{A(B)}$ ($\mathbf{k} \parallel \mathbf{L}$), although the sum over the two sublattices of the latter vanishes as discussed above. In Fig. 4 we consider four different settings: i) full Hamiltonian, ii) no valence $3d$ SOC, iii) no core-valence interaction beyond monopole (e.g. no spin exchange), iv) a combination of (ii) and (iii).

For $\mathbf{k} \parallel \mathbf{L}$, the valence $3d$ SOC plays a negligible role. The core-valence multipole interaction changes the shape of the single-site XMCD spectra, but does not change the magnitude of the effect. For $\mathbf{k} \perp \mathbf{L}$, we find a moderate difference between (i) and (ii). The single-site XMCD signal is substantially suppressed in (iii) and vanished completely in (iv). This shows that the role of the valence $3d$ SOC is marginal, while the core-valence multipole interaction is crucial for XMCD in α-MnTe.

The order of magnitude difference between the single-site XMCD for $\mathbf{k} \parallel \mathbf{L}$ and $\mathbf{k} \perp \mathbf{L}$, as well as their qualitatively different behavior in case (iv), suggest a different microscopic origin. The single-site XMCD for $\mathbf{k} \parallel \mathbf{L}$ corresponds to the conventional XMCD known from ferromagnets, which arises from the spin polarization of the valence states and SOC in the core states while the role of valence $3d$ SOC and core-valence interaction is marginal [45].

To microscopically understand the XMCD for $\mathbf{k} \perp \mathbf{L}$ in α-MnTe, we have to answer the question: *What is the symmetry origin of vanishing of XMCD in case (iv)?* We use the atomic model for sake of simplicity, nevertheless, the same symmetry arguments apply to the full Hamiltonian of α-MnTe. The terms corresponding to case (iv) are included in

$$\begin{aligned}\hat{H}^0_{\rm at} = \epsilon_c \sum_{m,\sigma} \hat{p}^\dagger_{m\sigma}\hat{p}_{m\sigma} + \sum_{m,m,\sigma,\sigma'} h^{(2\rm p)}_{m\sigma,m'\sigma'}\hat{p}^\dagger_{m\sigma}\hat{p}_{m'\sigma'} \\ + \sum_{m,m',\sigma} h^{(\rm CF)}_{mm'}\hat{d}^\dagger_{m\sigma}\hat{d}_{m'\sigma} + b\sum_{m,\sigma}\hat{d}^\dagger_{m\sigma}\hat{d}_{m-\sigma} \\ + U_{pd}\hat{n}_p\hat{n}_d + \sum_{\substack{i,j,k,l\\ \sigma,\sigma'}} u^{\sigma\sigma'}_{ijkl}\hat{d}^\dagger_{i\sigma}\hat{d}^\dagger_{j\sigma'}\hat{d}_{k\sigma'}\hat{d}_{l\sigma}.\end{aligned} \tag{1}$$

The remaining terms to complete the full atomic-model are

$$\hat{H}^1_{\rm at} = \sum_{\substack{i,j,k,l\\ \sigma,\sigma'}} w^{\sigma\sigma'}_{ijkl}\hat{d}^\dagger_{i\sigma}\hat{p}^\dagger_{j\sigma'}\hat{d}_{k\sigma'}\hat{p}_{l\sigma} + \sum_{\substack{m,m'\\ \sigma,\sigma'}} h^{(3\rm d)}_{m\sigma,m'\sigma'}\hat{d}^\dagger_{m\sigma}\hat{d}_{m'\sigma'}.$$

Here, the operators $\hat{p}^\dagger_{m\sigma}$ and $\hat{d}^\dagger_{m\sigma}$, respectively, create an electron in a core ($2p$) and valence ($3d$) orbital with angular momentum projection m and spin projection $\sigma = \pm 1$. The magnetic order is represented by a Weiss field b [46], chosen to point along the x-axis, without loss of generality.

The XMCD signal for $\mathbf{k} \perp \mathbf{L}$ (which is related to the antisymmetric part of σ_{xy}) is obtained by the Fermi's golden rule

$$\begin{aligned}F_\pm(\omega) &= \sum_{f,i} \left|\left\langle f|\hat{T}_\pm|i\right\rangle\right|^2 \delta\left(\omega - E_{fi}\right) \\ \hat{T}_\pm &\equiv \sum_\sigma \hat{T}^\sigma_\pm = \sum_{m,\sigma} \Gamma_{\pm m}\hat{d}^\dagger_{m\pm1\sigma}\hat{p}_{m\sigma} + H.c.\end{aligned} \tag{2}$$

where $E_{fi} = E_f - E_i$ is the excitation energy from the state $|i\rangle$ to state $|f\rangle$. The dipole operators $\hat{T}_\pm$, with real coefficients Γ_m, describe absorption of circularly polarized light propagating along the c-axis. The square of the matrix element in (2) has the form

$$\left|\left\langle \hat{T}_\pm \right\rangle\right|^2 = \sum_\sigma \left|\left\langle \hat{T}^\sigma_\pm \right\rangle\right|^2 + \sum_\sigma \left\langle \hat{T}^\sigma_\pm \right\rangle \overline{\left\langle \hat{T}^{-\sigma}_\pm \right\rangle}. \tag{3}$$

First, we use the local $\mathcal{C}_3$ rotation symmetry about the c-axis to show that the second term in (3) does not contribute to $F_\pm(\omega)$. Consider the $\mathcal{C}_3$ transformation acting only on the valence orbital indices (valence SOC neglected), and on both the core orbital and spin indices (core SOC included) [47]. This operation commutes with $\hat{H}^0_{\rm at}$ and thus

$$F_\pm(\omega) = \tfrac{1}{3}\sum_{g\in\{I,\mathcal{C}_3,\mathcal{C}_3^2\}} \sum_{f,i} \left|\left\langle f|g\hat{T}_\pm g^{-1}|i\right\rangle\right|^2 \delta\left(\omega - E_{fi}\right). \tag{4}$$

The transformation of the dipole operator

$$\mathcal{C}_3\hat{T}^\sigma_\pm\mathcal{C}_3^{-1} = \varepsilon\hat{T}^\sigma_\pm e^{-i\sigma\frac{\pi}{3}}, \tag{5}$$

introduces a spin-dependent phase shift (ε is an overall phase factor) arising from the phase difference between the valence spins (not rotated) and the core spins (rotated). As a result the crossed spin term in (3) drops out upon the summation in (4).

Next, we consider the role of $\mathcal{T}$. The $\mathcal{T}$-symmetry is broken by the presence of the Weiss field b. However, since the valence spin is coupled neither to the valence orbitals, nor to the core spin or orbitals, the transformation $\mathcal{T}' \equiv \mathcal{T}\mathcal{C}_2^{S,3d}$ [48] ($\mathcal{T}$ combined with a $\mathcal{C}_2^{S,3d}$ rotation of the valence spin) is an anti-unitary symmetry, see SM [43] for details, which transforms the dipole operators as

$$\mathcal{T}'\hat{T}^\sigma_\pm\mathcal{T}'^{-1} = (-1)^{\frac{\sigma-1}{2}}\hat{T}^\sigma_\mp. \tag{6}$$

As a result we can replace

$$\left\langle f|\hat{T}^\sigma_+|i\right\rangle \to (-1)^{\frac{\sigma-1}{2}}\overline{\left\langle f|\hat{T}^\sigma_-|i\right\rangle} \tag{7}$$

in the sum over eigenstates (2), which together with vanishing spin-crossed terms in (7), leads to $F_+(\omega) = F_-(\omega)$, and thus zero XMCD.

Turning on either of the terms in $\hat{H}^1_{\rm at}$ eliminates the above symmetries, and the arguments for zero XMCD

break down. However, for $\mathbf{L} \parallel [11\bar{2}0]$, XMCD for the full Hamiltonian $\hat{H}^0_{\rm at} + \hat{H}^1_{\rm at}$ still vanishes. Because of the presence of a mirror plane $\mathcal{M}$ perpendicular to $\mathbf{L}$, see Fig. 1, the Hamiltonian is invariant under $m \to -m$ and $\sigma \to -\sigma$ transformations for both valence and core orbitals. The $\mathcal{M}\hat{T}_+\mathcal{M}^{-1} = \hat{T}_-$ then implies vanishing of XMCD for $\mathbf{L} \parallel [11\bar{2}0]$.

Although both AHE and XMCD are given by the antisymmetric components of (frequency-dependent) $\sigma_{\alpha\beta}$, they arise from different terms in the Hamiltonian. AHE originates from SOC in the valence orbitals, i.e., the same interaction responsible for example for magnetocrystalline anisotropy. The electron-electron interactions tend to play a minor role for AHE [49], beyond establishing the magnetic order. XMCD in α-MnTe, on the other hand, shows little sensitivity to valence SOC, but arises from a combination of core SOC and core-valence exchange interaction, which affect the excited state containing a core hole. Only a minor modification of the XMCD signal is observed when the relativistic effects in the valence orbitals are completely neglected.

In conclusion, we have calculated XAS and XMCD at the Mn $L_{2,3}$ edge in a prototypical altermagnet α-MnTe. We have measured XAS and found a good agreement with the numerical results, establishing the reliability of the theoretical approach. The magnitude of calculated XMCD is well within the resolution of present-day instruments. The effect follows the same symmetry rules as established for AHE. In α-MnTe, it is present for the circularly polarized X-rays propagating along the c-axis and the Néel vector in the plane perpendicular to the c-axis. Within the plane, the effect vanishes for $\mathbf{L} \parallel [2\bar{1}\bar{1}0]$ and the other two equivalent in-plane axes. Unlike AHE, SOC in the valence orbitals plays only a marginal role for XMCD in α-MnTe.

We thank Jakub Železný, Satya Prakash Bommanaboyena and Anna Kauch for discussions and critical reading of the manuscript. This work was supported by JSPS KAKENHI Grant Numbers 21K13884, 21H01003, 23K03324, 23H03816, 23H03817 (A.H.), projects P30960-N27, I 4493-N (G.S.) and QUASTFOR5249 project I 5868-N (J.K.) of the Austrian Science Fund (FWF), the Czech Academy of Sciences, project LQ100102201 (D.K.) and project 22-22000M of the Czech Science Foundation (GACR), and Johannes Gutenberg University Grant TopDyn (L.Š).

[1] L. Šmejkal, A. H. MacDonald, J. Sinova, S. Nakatsuji, and T. Jungwirth, Nat. Rev. Mater. **7**, 482 (2022).
[2] L. Šmejkal, J. Sinova, and T. Jungwirth, Phys. Rev. X **12**, 040501 (2022).
[3] L. Šmejkal, R. González-Hernández, T. Jungwirth, and J. Sinova, Sci. Adv. **6**, eaaz8809 (2020).
[4] K. Samanta, M. Ležaić, M. Merte, F. Freimuth, S. Blügel, and Y. Mokrousov, J. Appl. Phys. **127**, 213904 (2020).
[5] M. Naka, S. Hayami, H. Kusunose, Y. Yanagi, Y. Motome, and H. Seo, Phys. Rev. B **102**, 075112 (2020).
[6] H. Reichlová, R. L. Seeger, R. González-Hernández, I. Kounta, R. Schlitz, D. Kriegner, P. Ritzinger, M. Lammel, M. Leiviskä, V. Petříček, P. Doležal, E. Schmoranzerová, A. Bad'ura, A. Thomas, V. Baltz, L. Michez, J. Sinova, S. T. B. Goennenwein, T. Jungwirth, and L. Šmejkal, arXiv:2012.15651.
[7] S. Hayami and H. Kusunose, Phys. Rev. B **103**, L180407 (2021).
[8] I. I. Mazin, K. Koepernik, M. D. Johannes, R. González-Hernández, and L. Šmejkal, Proc. Natl. Acad. Sci. U.S.A. **118**, e2108924118 (2021).
[9] R. D. Gonzalez Betancourt, J. Zubáč, R. Gonzalez-Hernandez, K. Geishendorf, Z. Šobáň, G. Springholz, K. Olejník, L. Šmejkal, J. Sinova, T. Jungwirth, S. T. B. Goennenwein, A. Thomas, H. Reichlová, J. Železný, and D. Kriegner, Phys. Rev. Lett. **130**, 036702 (2023).
[10] M. Naka, Y. Motome, and H. Seo, Phys. Rev. B **106**, 195149 (2022).
[11] M. Naka, S. Hayami, H. Kusunose, Y. Yanagi, Y. Motome, and H. Seo, Nat. Commun. **10**, 4305 (2019).
[12] R. González-Hernández, L. Šmejkal, K. Výborný, Y. Yahagi, J. Sinova, T. c. v. Jungwirth, and J. Železný, Phys. Rev. Lett. **126**, 127701 (2021).
[13] M. Naka, Y. Motome, and H. Seo, Phys. Rev. B **103**, 125114 (2021).
[14] H.-Y. Ma, M. Hu, N. Li, J. Liu, W. Yao, J.-F. Jia, and J. Liu, Nat. Commun. **12**, 2846 (2021).
[15] L. Šmejkal, A. B. Hellenes, R. González-Hernández, J. Sinova, and T. Jungwirth, Phys. Rev. X **12**, 011028 (2022).
[16] L. Šmejkal, J. Sinova, and T. Jungwirth, Phys. Rev. X **12**, 031042 (2022).
[17] K.-H. Ahn, A. Hariki, K.-W. Lee, and J. Kuneš, Phys. Rev. B **99**, 184432 (2019).
[18] S. Hayami, Y. Yanagi, and H. Kusunose, J. Phys. Soc. Jpn. **88**, 123702 (2019).
[19] L.-D. Yuan, Z. Wang, J.-W. Luo, E. I. Rashba, and A. Zunger, Phys. Rev. B **102**, 014422 (2020).
[20] L.-D. Yuan, Z. Wang, J.-W. Luo, and A. Zunger, Phys. Rev. Mater. **5**, 014409 (2021).
[21] S. Hayami, Y. Yanagi, and H. Kusunose, Phys. Rev. B **102**, 144441 (2020).
[22] P. Liu, J. Li, J. Han, X. Wan, and Q. Liu, Phys. Rev. X **12**, 021016 (2022).
[23] J. Yang, Z.-X. Liu, and C. Fang, arXiv:2105.12738.
[24] Z. Feng, X. Zhou, L. Šmejkal, L. Wu, Z. Zhu, H. Guo, R. González-Hernández, X. Wang, H. Yan, P. Qin, X. Zhang, H. Wu, H. Chen, Z. Meng, L. Liu, Z. Xia, J. Sinova, T. Jungwirth, and Z. Liu, Nat. Electron. **5**, 735 (2022).
[25] D.-F. Shao, S.-H. Zhang, M. Li, C.-B. Eom, and E. Y. Tsymbal, Nat. Commun. **12**, 7061 (2021).
[26] A. Bose, N. J. Schreiber, R. Jain, D.-f. Shao, H. P. Nair, J. Sun, X. S. Zhang, D. A. Muller, E. Y. Tsymbal, D. G. Schlom, and D. C. Ralph, Nat. Electron. **5**, 263 (2022), 2108.09150.
[27] H. Bai, L. Han, X. Y. Feng, Y. J. Zhou, R. X. Su, Q. Wang, L. Y. Liao, W. X. Zhu, X. Z. Chen, F. Pan, X. L. Fan, and C. Song, Phys. Rev. Lett. **128**, 197202 (2022).
[28] S. Karube, T. Tanaka, D. Sugawara, N. Kadoguchi,

M. Kohda, and J. Nitta, Phys. Rev. Lett. **129**, 137201 (2022).
[29] S. Wimmer, S. Mankovsky, J. Minár, A. N. Yaresko, and H. Ebert, Phys. Rev. B **100**, 214429 (2019).
[30] M. Kimata, N. Sasabe, K. Kurita, Y. Yamasaki, C. Tabata, Y. Yokoyama, Y. Kotani, M. Ikhlas, T. Tomita, K. Amemiya, H. Nojiri, S. Nakatsuji, T. Koretsune, H. Nakao, T.-h. Arima, and T. Nakamura, Nat. Commun. **12**, 5582 (2021).
[31] L. Šmejkal, J. Železný, J. Sinova, and T. Jungwirth, Phys. Rev. Lett. **118**, 106402 (2017).
[32] H. J. Elmers, S. V. Chernov, S. W. D'Souza, S. P. Bommanaboyena, S. Y. Bodnar, K. Medjanik, S. Babenkov, O. Fedchenko, D. Vasilyev, S. Y. Agustsson, C. Schlueter, A. Gloskovskii, Y. Matveyev, V. N. Strocov, Y. Skourski, L. Šmejkal, J. Sinova, J. Minár, M. Kläui, G. Schönhense, and M. Jourdan, ACS Nano **14**, 17554 (2020), pMID: 33236903, https://doi.org/10.1021/acsnano.0c08215.
[33] P. Villars and K. Cenzual, MnTe Crystal Structure: PAULING FILE Multinaries Edition – 2012, Berlin Heidelberg & Material Phases Data System (MPDS), Switzerland & National Institute for Materials Science (NIMS), Japan.
[34] A. Hariki, T. Uozumi, and J. Kuneš, Phys. Rev. B **96**, 045111 (2017).
[35] A. Hariki, M. Winder, and J. Kuneš, Phys. Rev. Lett. **121**, 126403 (2018).
[36] A. Hariki, M. Winder, T. Uozumi, and J. Kuneš, Phys. Rev. B **101**, 115130 (2020).
[37] P. Blaha, K. Schwarz, G. Madsen, D. Kvasnicka, and J. Luitz, *WIEN2k, An Augmented Plane Wave + Local Orbitals Program for Calculating Crystal Properties (Karlheinz Schwarz, Techn. Universitat Wien, Austria, 2001), ISBN 3-9501031-1-2*.
[38] J. Kuneš, R. Arita, P. Wissgott, A. Toschi, H. Ikeda, and K. Held, Comput. Phys. Commun. **181**, 1888 (2010).
[39] A. A. Mostofi, J. R. Yates, G. Pizzi, Y.-S. Lee, I. Souza, D. Vanderbilt, and N. Marzari, Comput. Phys. Commun. **185**, 2309 (2014).
[40] H. Sato, A. Tanaka, A. Furuta, S. Senba, H. Okuda, K. Mimura, M. Nakatake, Y. Ueda, M. Taniguchi, and T. Jo, J. Phys. Soc. Japan **68**, 2132 (1999).
[41] P. E. Faria Junior, K. A. de Mare, K. Zollner, K.-h. Ahn, S. I. Erlingsson, M. van Schilfgaarde, and K. Výborný, Phys. Rev. B **107**, L100417 (2023).
[42] J. Yi, X. He, and Y. Sun, J. Alloys Compd. **491**, 436 (2010).
[43] See Supplementary Material for details at ...
[44] D. Kriegner, H. Reichlova, J. Grenzer, W. Schmidt, E. Ressouche, J. Godinho, T. Wagner, S. Y. Martin, A. B. Shick, V. V. Volobuev, G. Springholz, V. Holý, J. Wunderlich, T. Jungwirth, and K. Výborný, Phys. Rev. B **96**, 214418 (2017).
[45] The core-valence interaction changes the shape of XMCD, primarily to due change of XAS.
[46] In AIM the Weiss field is represented by a spin-dependent bath.
[47] $\mathcal{C}_3\hat{p}_{m\sigma}\mathcal{C}_3^{-1} = e^{-i(2m+\sigma)\frac{\pi}{3}}\hat{p}_{m\sigma}$, $\mathcal{C}_3\hat{d}_{m\sigma}\mathcal{C}_3^{-1} = e^{-im\frac{2\pi}{3}}\hat{d}_{m\sigma}$.
[48] $\mathcal{T}'\hat{d}_{m\sigma}\mathcal{T}'^{-1} = (-1)^m\hat{d}_{-m-\sigma}$,
$\mathcal{T}'\hat{p}_{m\sigma}\mathcal{T}'^{-1} = (-1)^{m+\frac{\sigma-1}{2}}\hat{p}_{-m-\sigma}$..
[49] S. Li and A. Levchenko, Phys. Rev. Lett. **124**, 156802 (2020).

Supplementary Material of "X-ray Magnetic Circular Dichroism in Altermagnetic α-MnTe"

A. Hariki,[1] T. Yamaguchi,[1] D. Kriegner,[2] K. W. Edmonds,[3] P. Wadley,[3] S. S. Dhesi,[4]
G. Springholz,[5] L. Šmejkal,[6,2] K. Výborný,[2] T. Jungwirth,[2,3] and J. Kuneš[7]

[1]*Department of Physics and Electronics, Graduate School of Engineering, Osaka Metropolitan University, 1-1 Gakuen-cho, Nakaku, Sakai, Osaka 599-8531, Japan*
[2]*Institute of Physics, Czech Academy of Sciences, Cukrovarnická 10, 162 00 Praha 6 Czech Republic*
[3]*School of Physics and Astronomy, University of Nottingham, Nottingham NG7 2RD, United Kingdom*
[4]*Diamond Light Source, Chilton OX11 0DE, United Kingdom*
[5]*Institute of Semiconductor and Solid State Physics, Johannes Kepler University Linz, Altenbergerstr. 69, 4040 Linz, Austria*
[6]*Institut für Physik, Johannes Gutenberg Universität Mainz, D-55099 Mainz, Germany*
[7]*Institute for Solid State Physics, TU Wien, 1040 Vienna, Austria*

A. LDA+DMFT calculation for Mn $L_{2,3}$ XAS and XMCD of α-MnTe

The LDA+DMFT calculation for Mn $L_{2,3}$-edge X-ray absorption spectroscopy (XAS) and X-ray magnetic circular dichroism (XMCD) spectra of α-MnTe proceeds in the two steps. Firstly, a standard LDA+DMFT calculation [1, 2] is performed with the same implementation of Refs. [3, 4]. Then, the Mn $L_{2,3}$-edge XAS and XMCD intensities are computed from the Anderson impurity model (AIM) with the LDA+DMFT hybridization densities $\Delta(\omega)$, where the Mn $2p$ core orbitals and core-valence interaction are included explicitly. In the first step, the LDA bands obtained with the WIEN2K package [5] are projected onto a tight-binding model spanning the Mn $3d$ and Te $5p$ bands [6, 7]. The LDA calculation is performed for NiAs structure (space group $P6_3/mmc$) with lattice parameters of $a = 4.14$ Å and $c = 6.71$ Å [8, 9]. The tight-binding model is then augmented by the electron-electron interaction within the Mn $3d$ shell. The interaction is parameterized by Hubbard $U = F_0$ and Hund's $J = (F_2 + F_4)/14$ parameters where F_0, F_2, and F_4 are the Slater integrals [10, 11]. Consulting with previous DFT-based and spectroscopy studies for the studied and typical divalent Mn compounds [12–16], we employ $U = 5.0$ eV and $J = 0.86$ eV in the present study. The continuous-time quantum Monte Carlo method with the hybridization expansion formalism [17–19] is used to solve the auxiliary AIMs for the two Mn sites in the DMFT self-consistent calculation. The valence spectral intensities and hybridization densities $\Delta(\omega)$ are computed on the real frequency axis after the self-energy is analytically continued using maximum entropy method [20, 21]. To account for the electron-electron interaction already included in the LDA description, the Mn $3d$ orbital energy is shifted from its LDA value by the double-counting correction $\mu_{\rm dc}$ [1, 22]. While several *ad hoc* schemes exist to determine $\mu_{\rm dc}$, we treat $\mu_{\rm dc}$ as an adjustable parameter fixed by comparison to the experimental band gap, valence-band and Mn $2p$ core-level XPS data [3, 23]. Figure 1 shows the LDA+DMFT valence-band spectra computed for different double-counting values $\mu_{\rm dc}$. The LDA+DMFT result implementing $\mu_{dc} = 22.5$ eV reproduces the experimental gap ($\sim 1.27 - 1.46$ eV) [24–26] reasonably well. Besides, the presence of incoherent spectral weight of the Mn $3d$ states around -8 eV is consistent with the early Mn L-edge resonant X-ray photoemission spectroscopy (XPS) studies [15, 27]. In all calculated $\mu_{\rm dc}$ values, the antiferromagnetically ordered state is stabilized in the LDA+DMFT self-consistent calculations.

To further support the used model parameters, we calculate Mn $2p$ XPS spectra of α-MnTe, see Fig. 1. In contrast to the Mn $2p$ XAS process where the Mn $2p$ core hole created by the X-rays is largely screened by an extra Mn $3d$ electron added on the X-ray excited site, a dynamical charge response from the valence electrons to the Mn site, traditionally called charge-transfer screening, affects substantially the Mn $2p$ XPS line shape [3, 13, 29]. Thus, the Mn $2p$ XPS features are more sensitive to the parameters in the lattice model above. The Mn $2p$ XPS spectra are calculated using the AIM with the LDA+DMFT hybridization densities $\Delta(\omega)$. Note that $\Delta(\omega)$ depends on two Mn sites in the antiferromagnetic order. We used the same form of the AIM Hamiltonian and computational methods used in Refs. [3, 4, 30]. In practice, $\Delta(\omega)$ obtained with the LDA+DMFT calculation are represented by 25 discretized bath states (per orbital and spin) in computing the spectral intensities with a configuration-interaction impurity solver. The LDA+DMFT result with the optimal double-counting value ($\mu_{\rm dc} = 22.5$ eV) reproduces the experimental Mn $2p$ XPS spectrum nicely, including the Mn $2p_{3/2}$ main-line and satellite splitting as well as fine features in the main line. The $\mu_{\rm dc} = 22.5$ eV value is used for the simulated results in the main texts.

The same AIMs with the LDA+DMFT densities $\Delta(\omega)$ are used for computing Mn $L_{2,3}$-edge XAS and XMCD. The

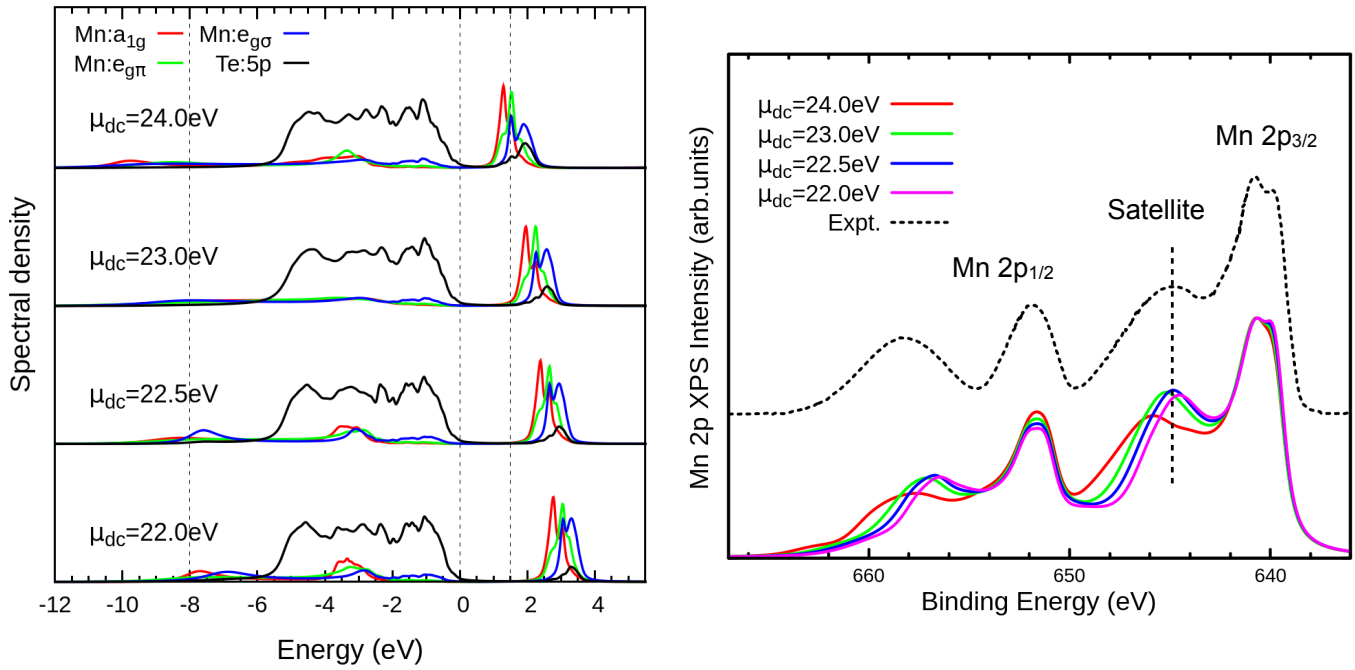

FIG. 1. (left) LDA+DMFT orbital-resolved density of states calculated for different double-counting values $\mu_{\rm dc}$. In the crystal structure of α–MnTe, the Mn $3d$ on-site levels are split into two doublets ($e_{g\pi}$, $e_{g\sigma}$) and a singlet (a_{1g}). (right) Mn $2p$ core-level XPS spectra calculated by the LDA+DMFT AIM method with these double-counting values $\mu_{\rm dc}$. The experimental XPS spectrum taken from Ref. [28] is shown together.

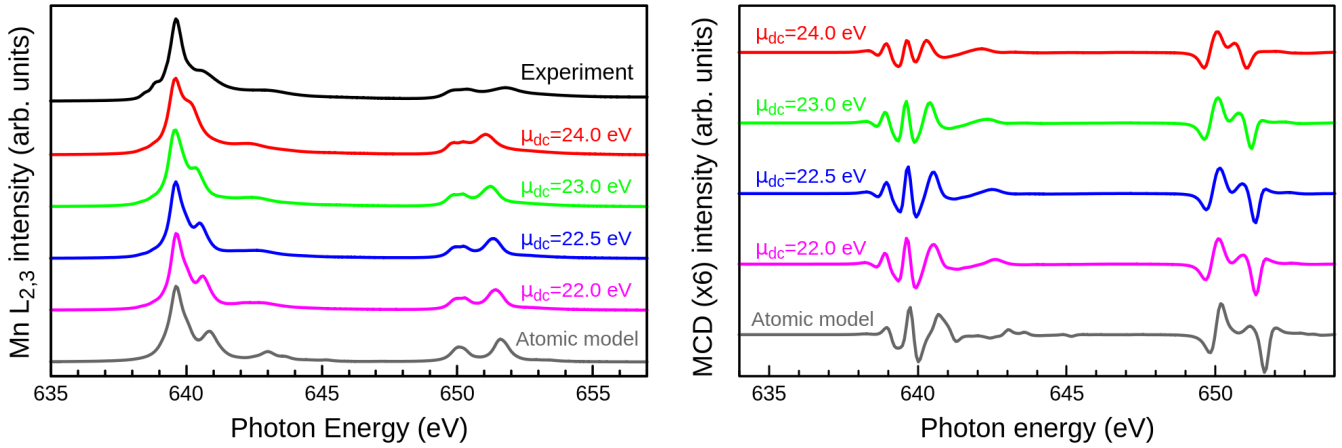

FIG. 2. (left) Mn $L_{2,3}$ XAS intensities calculated by the LDA+DMFT AIM for different double-counting values $\mu_{\rm dc}$. The experimental spectrum in Fig. 1 of the main text is shown. (right) Mn $L_{2,3}$ MCD intensities ($\times 6$) computed for these $\mu_{\rm dc}$ values. For comparison, the XAS and XMCD intensities calculated by the Mn^{2+} atomic model are shown together (gray).

XAS spectral function is described by the Fermi's golden rule

$$F^{(i)}_{\rm XAS}(\omega_{\rm in}) = -\frac{1}{\pi}\,{\rm Im}\langle g|T_{\rm i}^{\dagger}\frac{1}{\omega_{\rm in}+E_g-\hat{H}^{(i)}_{\rm AIM}}T_{\rm i}|g\rangle.$$

Here, $|g\rangle$ is the ground with energy E_g, and $\omega_{\rm in}$ is the energy of the incident photon. $T_{\rm i}$ is the electric dipole transition operator for circularly- or linearly-polarized X-rays [29, 31]. The index i ($=1,2$) denotes the X-ray excited Mn site in the unit cell. The AIM Hamiltonian $\hat{H}^{(i)}_{\rm AIM}$ contains the site-dependent DMFT hybridization densities $\Delta(\omega)$, the Mn $3d$-shell atomic Hamiltonian, the core-valence interaction with the Mn $2p$ core states, and the spin-orbital coupling on the Mn $2p$ and $3d$ shells. The AIM for each Mn site is used to calculate the site contributions, and then the total

XAS and XMCD intensities are obtained by summing up the two-site contributions [4]. The spectral broadening using a Lorentizan 400 meV and a Gaussian 100 meV (FWHM) is applied in the XAS and XMCD spectra to simulate $2p$ core-hole lifetime broadening and experimental instrumental broadening. We demonstrated in Fig. 2 that the double-counting value $\mu_{\rm dc}$ has little effect on the Mn $L_{2,3}$ XMCD intensities in α-MnTe. In Fig. 2, we also show XAS and XMCD intensities calculated by a Mn^{2+} atomic model that implements the same local Hamiltonian with the LDA+DMFT AIM but neglects the hybridization with the bath orbitals. The Mn^{2+} atomic model gives similar XAS and XMCD spectra with the LDA+DMFT AIM. The absorption of a core-level electron to the valence state is a local excitation (forming a bound exciton between the core hole and Mn $3d$ electrons on the X-ray excited site) and the Mn $2p$ core-hole does not leave the excited Mn site. Thus, the single impurity model, even the atomic model, provides its good description [4, 29, 32]. The Mn $L_{2,3}$ XAS spectrum of MnTe exhibits rich multiplet features characteristic for a Mn^{2+} ion with a moderate crystal field potential acting on the Mn $3d$ shell [32]. The present LDA+DMFT as well as the atomic model calculation underestimates the intensity of the shoulder feature around 641 eV which is known to be sensitive to a small change in the crystal field splitting [32]. Thus, the discrepancy is most likely due to an underestimate of the crystal field splitting in the LDA Hamiltonian as discussed in Refs. [23, 33]

I. SYMMETRY CONSIDERATIONS

Here, we provide explicit form of the bilinear part of the atomic Hamiltonian in the angluar momentum (spherical harmonics) basis with quantization axis along the crystallographic c-axis. The form of the crystal-field Hamiltonian $h^{\rm CF}$ in angular momentum basis $|m_l, m_s\rangle$ ($m_l = 1, 0, -1$ for $2p$ and $m_l = 2, 1, 0, -1, -2$ for $3d$, and $m_s = 1/2, -1/2$ for spin) implied by the 3-fold rotation axis ($m - m' = 3k$ for $h^{\rm CF}_{mm'}$ to be non-zero) and $\mathcal{T}$-reversal symmetry ($h^{\rm CF}_{-m-m'} = (-1)^{m+m'}\overline{h^{\rm CF}_{mm'}}$)

$$h^{\rm CF} = \left(\begin{array}{ccccc|ccccc} a & 0 & 0 & x & 0 & & & & & \\ 0 & b & 0 & 0 & -\bar{x} & & & & & \\ 0 & 0 & c & 0 & 0 & & & \mathbf{0} & & \\ \bar{x} & 0 & 0 & b & 0 & & & & & \\ 0 & -x & 0 & 0 & a & & & & & \\ \hline & & & & & a & 0 & 0 & x & 0 \\ & & & & & 0 & b & 0 & 0 & -\bar{x} \\ & & \mathbf{0} & & & 0 & 0 & c & 0 & 0 \\ & & & & & \bar{x} & 0 & 0 & b & 0 \\ & & & & & 0 & -x & 0 & 0 & a \end{array}\right).$$

Presence of $\mathcal{M}_x$ ($h^{\rm CF}_{-m-m'} = h^{\rm CF}_{mm'}$) would further reduce x to be purely imaginary. For MnTe, $a = 0.024$ eV, $b = 0.064$ eV, $c = -0.177$ eV, and $x = \overline{x} = 0.056$ eV are found in the tight-binding Hamiltonian constructed from the LDA bands. The spin-orbit coupling on the Mn $2p$ and $3d$ shell has the form of $h^{\rm soc}_{2p}$ and $h^{\rm soc}_{3d}$ in angular momentum basis,

$$h^{\rm SOC}_{2p} = \frac{\xi_{2p}}{2}\left(\begin{array}{ccc|ccc} 1 & 0 & 0 & 0 & 0 & 0 \\ 0 & 0 & 0 & \sqrt{2} & 0 & 0 \\ 0 & 0 & -1 & 0 & \sqrt{2} & 0 \\ \hline 0 & \sqrt{2} & 0 & -1 & 0 & 0 \\ 0 & 0 & \sqrt{2} & 0 & 0 & 0 \\ 0 & 0 & 0 & 0 & 0 & 1 \end{array}\right).$$

and

$$h^{\rm SOC}_{3d} = \frac{\xi_{3d}}{2}\left(\begin{array}{ccccc|ccccc} 2 & 0 & 0 & 0 & 0 & 0 & 0 & 0 & 0 & 0 \\ 0 & 1 & 0 & 0 & 0 & 2 & 0 & 0 & 0 & 0 \\ 0 & 0 & 0 & 0 & 0 & 0 & \sqrt{6} & 0 & 0 & 0 \\ 0 & 0 & 0 & -1 & 0 & 0 & 0 & \sqrt{6} & 0 & 0 \\ 0 & 0 & 0 & 0 & -2 & 0 & 0 & 0 & 2 & 0 \\ \hline 0 & 2 & 0 & 0 & 0 & -2 & 0 & 0 & 0 & 0 \\ 0 & 0 & \sqrt{6} & 0 & 0 & 0 & -1 & 0 & 0 & 0 \\ 0 & 0 & 0 & \sqrt{6} & 0 & 0 & 0 & 0 & 0 & 0 \\ 0 & 0 & 0 & 0 & 2 & 0 & 0 & 0 & 1 & 0 \\ 0 & 0 & 0 & 0 & 0 & 0 & 0 & 0 & 0 & 2 \end{array}\right),$$

where the spin-orbit coupling constant values ξ_{2p} and ξ_{3d} are 6.846 eV and 0.040 eV in the Mn^{2+} atomic Hamiltonian, respectively.

Transformation of dipole element under anti-unitary transformation $\mathcal{T}'$

$$\begin{aligned}
\left\langle f|\hat{T}_+^\sigma|i\right\rangle &= \overline{\left\langle \mathcal{T}'f|\mathcal{T}'\hat{T}_+^\sigma|i\right\rangle} && \text{anti-unitarity}\\
&= \overline{\left\langle \mathcal{T}'f|\mathcal{T}'\hat{T}_+^\sigma\mathcal{T}'^{-1}|\mathcal{T}'i\right\rangle} && \text{insertion of unity}\\
&= (-1)^{\frac{\sigma-1}{2}}\overline{\left\langle \mathcal{T}'f|\hat{T}_-^\sigma|\mathcal{T}'i\right\rangle}\\
\sum_{f,i}\left|\left\langle f|\hat{T}_+^\sigma|i\right\rangle\right|^2\delta(\omega-E_{fi}) &= \sum_{f,i}\left|\overline{\left\langle f|\hat{T}_-^\sigma|i\right\rangle}\right|^2\delta(\omega-E_{fi}) \qquad \mathcal{T}'\hat{H}^0_{\rm at}\mathcal{T}'^{-1}=\hat{H}^0_{\rm at} \quad \hat{H}^0_{\rm at}|\mathcal{T}'f\rangle = E|\mathcal{T}'f\rangle
\end{aligned}$$

In the last line we use the fact that the sum is invariant under arbitrary unitary transformation in the eigensubspaces of $\hat{H}$.

The $\mathcal{T}$-symmetry of $h^{\rm CF}$ is implemented by $h^{\rm CF}_{-m,-m'}=(-1)^{m+m'}(h^{\rm CF}_{m,m'})^*$. Therefore

$$\begin{aligned}
\mathcal{T}\hat{H}^{\rm CF}\mathcal{T}^{-1} &= \mathcal{T}h^{\rm CF}_{m,m'}\hat{d}^\dagger_m\hat{d}_{m'}\mathcal{T}^{-1}\\
&= (h^{\rm CF}_{m,m'})^*\mathcal{T}\hat{d}^\dagger_m\hat{d}_{m'}\mathcal{T}^{-1}\\
&= (h^{\rm CF}_{m,m'})^*(-1)^{m+m'}\hat{d}^\dagger_{-m}\hat{d}_{-m'}\\
&= \hat{H}^{\rm CF}
\end{aligned}$$

The invariance of $\hat{H}^{\rm CF}$ under $\mathcal{T}$ (and therefore $\mathcal{T}'$) leads to the $\mathcal{T}'$-invariance of $\hat{H}^0_{\rm at}$.

[1] G. Kotliar, S. Y. Savrasov, K. Haule, V. S. Oudovenko, O. Parcollet, and C. A. Marianetti, Rev. Mod. Phys. **78**, 865 (2006).
[2] A. Georges, G. Kotliar, W. Krauth, and M. J. Rozenberg, Rev. Mod. Phys. **68**, 13 (1996).
[3] A. Hariki, T. Uozumi, and J. Kuneš, Phys. Rev. B **96**, 045111 (2017).
[4] M. Winder, A. Hariki, and J. Kuneš, Phys. Rev. B **102**, 085155 (2020).
[5] P. Blaha, K. Schwarz, G. Madsen, D. Kvasnicka, and J. Luitz, *WIEN2k, An Augmented Plane Wave + Local Orbitals Program for Calculating Crystal Properties (Karlheinz Schwarz, Techn. Universitat Wien, Austria, 2001), ISBN 3-9501031-1-2*.
[6] A. A. Mostofi, J. R. Yates, G. Pizzi, Y.-S. Lee, I. Souza, D. Vanderbilt, and N. Marzari, Comput. Phys. Commun. **185**, 2309 (2014).
[7] J. Kuneš, R. Arita, P. Wissgott, A. Toschi, H. Ikeda, and K. Held, Comput. Phys. Commun. **181**, 1888 (2010).
[8] D. Kriegner, H. Reichlova, J. Grenzer, W. Schmidt, E. Ressouche, J. Godinho, T. Wagner, S. Y. Martin, A. B. Shick, V. V. Volobuev, G. Springholz, V. Holý, J. Wunderlich, T. Jungwirth, and K. Výborný, Phys. Rev. B **96**, 214418 (2017).
[9] S. Greenwald, Acta Cryst. **6**, 396 (1953).
[10] E. Pavarini, E. Koch, A. Lichtenstein, and D. E. Vollhardt, *The LDA+DMFT approach to strongly correlated materials*, Schriften des Forschungszentrums Jülich : Modeling and Simulation, Vol. 1 (2011) record converted from VDB: 12.11.2012.
[11] E. Pavarini, "Electronic Structure Calculations with LDA+DMFT," in *Many-Electron Approaches in Physics, Chemistry and Mathematics, Mathematical Physics Studies, ISBN 978-3-319-06378-2. Springer International Publishing Switzerland, 2014, p. 321*, edited by V. Bach and L. Delle Site (2014) p. 321.
[12] A. V. Kuneš, Lukoyanov, V. I. Anisimov, R. T. Scalettar, and W. E. Pickett, Nat. Mater. **7**, 198 (2008).
[13] A. E. Bocquet, T. Mizokawa, T. Saitoh, H. Namatame, and A. Fujimori, Phys. Rev. B **46**, 3771 (1992).
[14] V. I. Anisimov, J. Zaanen, and O. K. Andersen, Phys. Rev. B **44**, 943 (1991).
[15] H. Sato, A. Tanaka, A. Furuta, S. Senba, H. Okuda, K. Mimura, M. Nakatake, Y. Ueda, M. Taniguchi, and T. Jo, J. Phys. Soc. Japan **68**, 2132 (1999).
[16] T. Kotsugi, H. Sato, S. Senba, H. Okuda, Y. Ueda, M. Taniguchi, Y. Harada, S. Shin, A. Tanaka, and T. Jo, J. Electron Spectrosc. Relat. Phenom **88-91**, 293 (1998).
[17] P. Werner, A. Comanac, L. de' Medici, M. Troyer, and A. J. Millis, Phys. Rev. Lett. **97**, 076405 (2006).
[18] L. Boehnke, H. Hafermann, M. Ferrero, F. Lechermann, and O. Parcollet, Phys. Rev. B **84**, 075145 (2011).
[19] H. Hafermann, K. R. Patton, and P. Werner, Phys. Rev. B **85**, 205106 (2012).
[20] X. Wang, E. Gull, L. de' Medici, M. Capone, and A. J. Millis, Phys. Rev. B **80**, 045101 (2009).
[21] M. Jarrell and J. Gubernatis, Phys. Rep. **269**, 133 (1996).

[22] M. Karolak, G. Ulm, T. Wehling, V. Mazurenko, A. Poteryaev, and A. Lichtenstein, J. Electron Spectrosc. Relat. Phenom. **181**, 11 (2010).
[23] A. Hariki, M. Winder, T. Uozumi, and J. Kuneš, Phys. Rev. B **101**, 115130 (2020).
[24] D. Kriegner, K. Výborný, K. Olejník, H. Reichlová, V. Novák, X. Marti, J. Gazquez, V. Saidl, P. Němec, V. V. Volobuev, G. Springholz, V. Holý, and T. Jungwirth, Nat. Commun. **7**, 11623 (2016).
[25] C. Ferrer-Roca, A. Segura, C. Reig, and V. Muñoz, Phys. Rev. B **61**, 13679 (2000).
[26] G. Zanmarchi, J. Phys. Chem. Solids **28**, 2123 (1967).
[27] Y. Ueda, H. Sato, M. Taniguchi, N. Happo, T. Mihara, H. Namatame, T. Mizokawa, and A. Fujimori, J. Condens. Matter Phys. **6**, 8607 (1994).
[28] R. Iwanowski, M. Heinonen, and B. Witkowska, J. Alloys Compd. **491**, 13 (2010).
[29] F. de Groot and A. Kotani, *Core Level Spectroscopy of Solids* (CRC Press, Boca Raton, FL, 2014).
[30] M. Ghiasi, A. Hariki, M. Winder, J. Kuneš, A. Regoutz, T.-L. Lee, Y. Hu, J.-P. Rueff, and F. M. F. de Groot, Phys. Rev. B **100**, 075146 (2019).
[31] M. Matsubara, T. Uozumi, A. Kotani, Y. Harada, and S. Shin, J. Phys. Soc. Jpn. **69**, 1558 (2000).
[32] F. M. F. de Groot, J. C. Fuggle, B. T. Thole, and G. A. Sawatzky, Phys. Rev. B **42**, 5459 (1990).
[33] M. W. Haverkort, M. Zwierzycki, and O. K. Andersen, Phys. Rev. B **85**, 165113 (2012).